Tectonophysics 439 (2010) 216–221

Contents lists available at ScienceDirect

Tectonophysics

journal homepage: www.elsevier.com/locate/tecto

Ground motion hazard from supershear rupture

D.J. Andrews

U. S. Geological Survey, Menlo Park, CA 94025, USA

ARTICLE INFO

Article history:
Received 13 July 2009
Received in revised form 28 January 2010
Accepted 8 February 2010
Available online 12 February 2010

Keywords:
Supershear rupture
Ground motion hazard

ABSTRACT

An idealized rupture, propagating smoothly near a terminal rupture velocity, radiates energy that is focused into a beam. For rupture velocity less than the S-wave speed, radiated energy is concentrated in a beam of intense fault-normal velocity near the projection of the rupture trace. Although confined to a narrow range of azimuths, this beam diverges and attenuates. For rupture velocity greater than the S-wave speed, radiated energy is concentrated in Mach waves forming a pair of beams propagating obliquely away from the fault. These beams do not attenuate until diffraction becomes effective at large distance. Events with supershear and sub-Rayleigh rupture velocity are compared in 2D plane-strain calculations with equal stress drop, fracture energy, and rupture length; only static friction is changed to determine the rupture velocity. Peak velocity in the sub-Rayleigh case near the termination of rupture is larger than peak velocity in the Mach wave in the supershear case. The occurrence of supershear rupture propagation reduces the most intense peak ground velocity near the fault, but it increases peak velocity within a beam at greater distances.

Published by Elsevier B.V.

1. Introduction

Andrews (1976) resolved a theoretical paradox between Kostrov (1970) and Burridge (1973) about the limiting rupture propagation velocity of a plane-strain shear crack, but that paper did not examine the ground motion produced by supershear rupture. The purpose of this paper is to correct that lack; it will compare the distribution of peak ground velocity for ruptures with supershear versus sub-Rayleigh propagation velocity in a simple idealized 2D model.

Supershear rupture was inferred from observations of the 1979 Imperial Valley earthquake (Archuleta, 1984; Spudich and Cranswick, 1984). Clear evidence of supershear rupture in a number of recent large strike–slip earthquakes has spurred efforts to model the ground motion. Dunham and Archuleta (2005) and Bernard and Baumont (2005) pointed out that the Mach S wave from a supershear rupture will carry the motion on the fault surface to large distances with no diminution of amplitude. Liu and Lapusta (2008) found that perturbations can cause a quicker transition to supershear rupture velocity than considered by Burridge (1973) and Andrews (1976). Dunham and Bhat (2008) examined both Mach S and Mach Rayleigh waves in 3D dynamic models with prescribed propagation of stress drop. Bizzarri and Spudich (2008) calculated spontaneous propagation models and used isochrone theory to examine how the transition between sub-Rayleigh and supershear propagation velocity affects the spectrum of high-frequency ground motion. They also note that curvature of the rupture front in 3D leads to attenuation of the Mach wave. Bizzarri et al. (2010) and Schmedes et al. (2009) are examining supershear rupture in models with realistic heterogeneous stress. In the midst of these and many more current modeling works, this paper will present a simple idealized comparison, not with the object of modeling realistic ground motion, but to gain physical insight.

2. An idealized model

The calculations done here are in plane-strain geometry and use essentially the same 2D finite difference code used by Andrews (1976).

The elastic medium is uniform with density 2700 kg/m^3, S-wave speed 3000 m/s, and P-wave speed 5196 m/s. The fault is straight, located at $y=0$ in the Cartesian x,y coordinate system. The initial normal compressive stress on the fault is 100 MPa, and the initial shear stress is 60 MPa. This initial stress state may be characterized by an 'initial friction' parameter $\mu_0=0.6$. The coefficient of static friction μ_s is larger than μ_0, and it differs in the cases calculated. In the region $-15\ \text{km}<x<45\ \text{km}$, the coefficient of kinetic friction μ_k is 0.5 in all cases, so that dynamic stress drop is 10 MPa. Outside this region, kinetic friction is equal to static friction, $\mu_k=\mu_s$ so that the rupture stops gradually. Rupture is nucleated at $x=0$ by forcing the stress drop to propagate bilaterally with a rupture velocity no less than 2000 m/s. After the rupture has grown sufficiently, it propagates spontaneously at faster velocity.

A slip-weakening friction law is used. The coefficient of friction decreases from μ_s to μ_k as slip increases from 0 to D_c.

Three calculations are done. Parameters of the three cases are tabulated in Table 1. Stress drop and fracture energy are the same in all cases, in the region in which stress drop occurs.

E-mail address: jandrews@usgs.gov.

0040-1951/$ – see front matter. Published by Elsevier B.V.
doi:10.1016/j.tecto.2010.02.003

Table 1

Case	Sub-Rayleigh	Supershear, hard stop	Supershear, soft stop
Static friction, inside	0.76	0.68	0.68
Kinetic friction, inside	0.5	0.5	0.5
Static friction, outside	0.76	0.76	0.68
Kinetic friction, outside	0.76	0.76	0.68
D_c	0.346 m	0.5 m	0.5 m
Potency	$1.20 \cdot 10^6$ m^3/m	$1.22 \cdot 10^6$ m^3/m	$1.48 \cdot 10^6$ m^3/m
Elastic energy released	66.3 TJ/m	67.3 TJ/m	82.8 TJ/m
Total friction work	61.1 TJ/m	62.2 TJ/m	77.0 TJ/m
Total fracture work	1.79 TJ/m	1.52 TJ/m	3.32 TJ/m
Radiated energy	3.42 TJ/m	3.58 TJ/m	2.46 TJ/m
Apparent stress	2.86 MPa	2.93 MPa	1.66 MPa

TJ: terajoules.

In the case labeled 'sub-Rayleigh', in the region -15 km$<x<45$ km, the coefficient of static friction is $\mu_s = 0.76$. The parameter $s = (\mu_s - \mu_0)/(\mu_0 - \mu_k) = 1.6$ is large enough that the rupture velocity remains less than the Rayleigh speed through the duration of this calculation. In this case, D_c is set to 0.346 m. In the two cases labeled 'supershear', static friction in the region -15 km$<x<45$ km is $\mu_s = 0.68$. The parameter $s = (\mu_s - \mu_0)/(\mu_0 - \mu_k) = 0.8$ is small enough that a transition to supershear rupture propagation occurs. In these cases, D_c is set to 0.5 m. In the region in which stress drops, the parameters are chosen such that the product $(\mu_s - \mu_k)\ D_c$, which is proportional to fracture energy, is the same in all cases.

Outside the interval -15 km$<x<45$ km, shear stress increases rather than drops as slip occurs, so that slip stops gradually. In the 'sub-Rayleigh' case, $\mu_k = \mu_s = 0.76$ in the outer region, so that static friction is the same as in the inner region. There are two supershear cases, with different choices of friction in the outer region. In the 'supershear, hard stop' case, $\mu_k = \mu_s = 0.76$ in the outer region, so that stopping is similar to the 'sub-Rayleigh' case. In the 'supershear, soft stop' case, $\mu_k = \mu_s = 0.68$, so that static friction is the same as in the inner region.

In crack-like models, such as this work, peak slip rate depends on stress drop and rupture velocity, but is independent of the rate of slip-weakening. This work focuses on peak velocity, which is not sensitive to the rate of stress drop, while peak acceleration is proportional to that rate. By contrast, in a pulse-like model, such as Dunham and Bhat (2008), peak velocity depends on the cohesive zone width.

3. Computational details

For the stress drop and fracture energy chosen here, the critical crack half-length is 928 m, which means that an initially static crack of greater length will grow spontaneously. These dynamically driven ruptures start to propagate spontaneously at distances somewhat greater than 1 km.

With a slip-weakening friction law with constant D_c, the width of the cohesive zone shrinks as the rupture lengthens. As the cohesive zone width approaches the discrete interval of the computational grid, artificial oscillation in the solution increases. In the supershear case, the cohesive zone width is about 250 m at 11 km, the distance at which the supershear transition starts. In order to have small artificial oscillation up to that point in the calculation, the grid interval is chosen to be 50 m. The grid extends 120 km in each direction from the nucleation point, so a grid of 4800 by 4800 elements is needed.

In this way, a smooth solution with constant fracture energy is achieved up to the point of the supershear transition. At greater rupture lengths, particularly in the sub-Rayleigh case, this grid interval is not fine enough to control the noise. In order to smooth the solution, the slip-weakening friction law is supplemented with time-weakening friction. The drop in friction can occur no faster than the time interval for an S wave to propagate 5 grid intervals, 0.083 s. This prescription increases the fracture energy, but, since the ruptures are already propagating near their terminal velocities, only very short wavelength components of the solution are affected. Using time-weakening is equivalent to using artificial viscosity to smooth the solution, except that it is applied only at the source of the noise, the rupture front.

These simulations are run to 30 s, with a time step of 0.0079 s. The time-weakening prescription smoothes the solution, but small amplitude noise remains with period of about 6 time steps. Results shown in the plots have been smoothed further with a 9-point box function. Some very sharp peaks are found in these idealized problems. The peaks that remain after the smoothing are credible. The effective sampling interval is 0.07 s, so the solutions are good down to 0.14 s period or up to 7 Hz in frequency.

These calculations are intended to simulate an ideal case with constant fracture energy, but that ideal case is not realistic. Inelastic deformation near the rupture front, which is not included in these calculations, contributes to fracture energy and increases as the rupture grows. In a crack-like solution with inelastic off-fault response, fracture energy is proportional to rupture length. Therefore, the nucleation length can be vanishingly small, the propagation distance at the supershear transition can be arbitrarily small, the cohesive zone grows as the rupture lengthens, and there is a limiting value of slip rate. When we numerical practitioners choose to use constant fracture energy for ruptures spanning large length scales, we are making unnecessary difficulties for ourselves, because the shrinking cohesive zone is not realistic.

4. Results

Before examining the dynamic motion, let us look at the overall size of these three events. Fig. 1a shows the final slip distributions, and

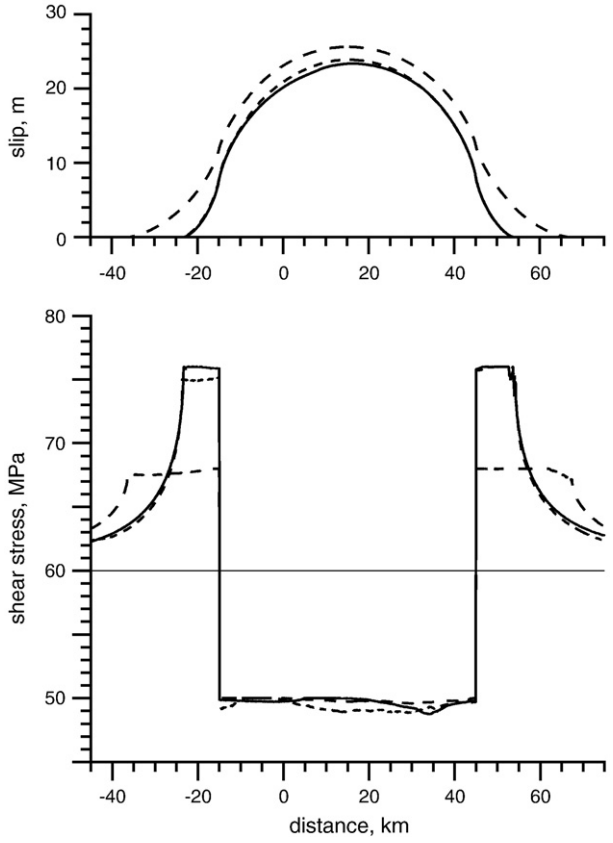

Fig. 1. Final slip (top) and final shear traction on fault (bottom) as a function of distance along the fault for the three cases calculated. Distance is measured from the nucleation point. Solid curves; sub-Rayleigh case, short-dashed curves: 'supershear, hard stop' case, long-dashed curves: 'supershear, soft stop' case. Light line is initial shear traction.

Fig. 1b shows the final shear traction on the fault in the three cases. The 'sub-Rayleigh' and 'supershear, hard stop' cases have very similar slip and final stress, because their stopping stress is the same. The 'supershear, soft stop' case has larger slip that penetrates farther into the barrier region. Table 1 shows potency and energy of the events per meter of thickness normal to the 2D plane. Potency in this 2D case is the integral of slip over the fault length. Friction work is defined as work done against the kinetic friction stress τ_k. Fracture work is defined as work done against the difference of instantaneous stress and kinetic fiction stress, $\tau - \tau_k$. Both the slip-weakening and time-weakening mechanisms contribute to fracture work. The time-weakening contribution is significant in the barrier region, where the fracture energy of slip-weakening is zero. Radiated energy is found as elastic energy released minus friction work minus fracture work. The 'sub-Rayleigh' and 'supershear, hard stop' cases have about the same potency and radiated energy. The 'supershear, soft stop' case has larger potency and smaller radiated energy.

The evolution of slip rate on the fault as a function of time for the 'sub-Rayleigh' case is shown in Fig. 2. The rupture propagates bilaterally very near the Rayleigh speed with peak slip rate increasing with propagation distance. The rupture stops at barriers beginning at −15 km and at +45 km.

The peak absolute value of each component of velocity is saved at each point of the grid for each calculation. Maps of the peak absolute values of the fault-parallel and fault-normal components are shown in Figs. 3 and 4, respectively, for the sub-Rayleigh case. The fault-normal component is large at the rupture front and grows with propagation distance until the barrier is met in the positive direction at 45 km. Slip is zero beyond 54 km, but strong fault-normal velocity is seen near the fault at larger distances. This directivity beam of peak ground velocity is concentrated at azimuths near the fault projection, but the beam diverges and attenuates with distance from the end of rupture. The termination of shading near 85 km is the S-wave front; peak velocity has not yet been reached at farther points.

Ground velocity can be examined more quantitatively in time history plots at selected points. Fault-normal velocity in the sub-Rayleigh case is plotted in Fig. 5 at two points on the projection of the fault and beyond the termination of slip. At point D1, located 60 km along strike, peak velocity is 4.55 m/s. At point D2, located 75 km along strike, peak velocity is 3.56 m/s. Peak velocity is attenuating, because the directivity beam is diverging.

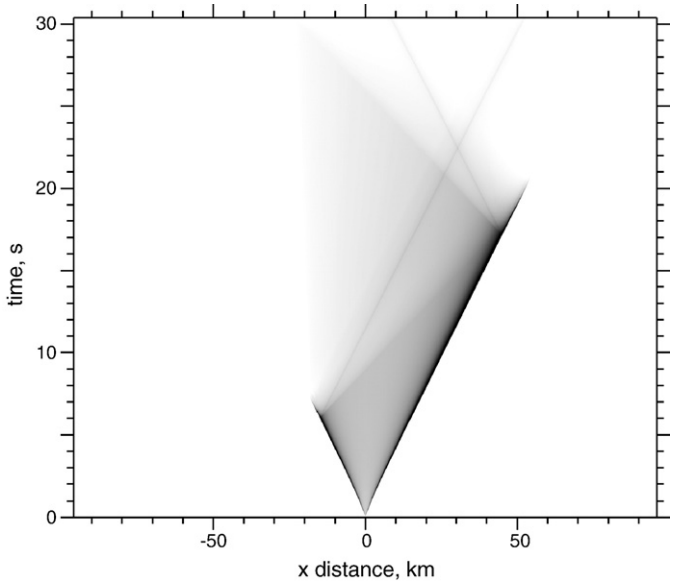

Fig. 2. Evolution of slip rate on the fault as a function of time in the sub-Rayleigh case. Darkest shading is slip rate of 5 m/s or greater.

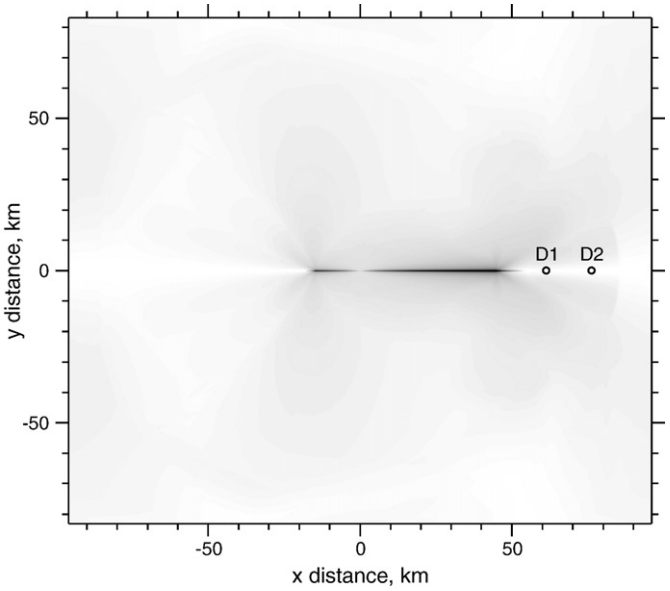

Fig. 3. Map of peak absolute value of the fault-parallel component of velocity in the sub-Rayleigh case, at times up to 30 s. The same gray scale is used in all figures. Darkest shading (not reached in this figure) is velocity of 5 m/s or greater. Points labeled D1 and D2 are locations of time histories shown in Fig. 5.

Fig. 6 shows slip rate on the fault in the 'supershear, soft stop' case. The rupture starts growing bilaterally near the Rayleigh speed. At 11 km the supershear transition starts with slip triggered at the S-wave front (with shading too faint to be seen in the figure). The transition is complete at 14 km. The supershear rupture front is promptly extinguished by the barrier at −15 km in the negative direction, but the supershear rupture propagates with increasing slip rate amplitude in the positive direction until the barrier is met at 45 km. The rupture front reaches a propagation velocity of 5030 m/s = 0.968 v_P = 1.677 v_S. At this velocity, the rupture generates a Mach S wave oriented at angle ϕ to the fault, where $\sin\phi = 1/1.677$, or $\phi = 36.6°$.

Maps of peak absolute value of ground velocity in the 'supershear, soft stop' case are shown in Fig. 7 for the fault-parallel component and in Fig. 8 for the fault-normal component. Energy is focused in a pair of

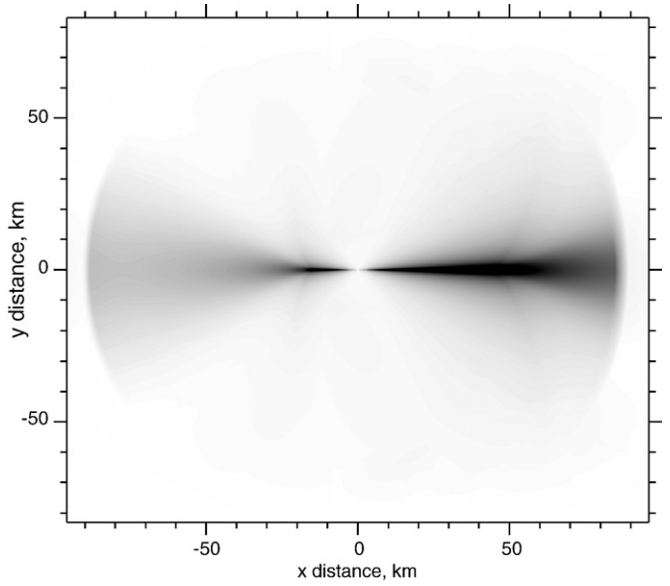

Fig. 4. Map of peak absolute value of the fault-normal component of velocity in the sub-Rayleigh case, at times up to 30 s. Darkest shading is velocity of 5 m/s or greater.

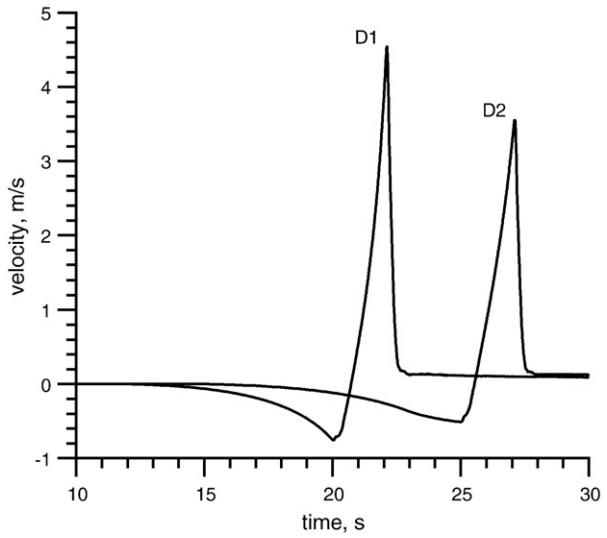

Fig. 5. Time histories of fault-normal velocity in the sub-Rayleigh case at points D1 and D2. Locations, shown in Fig. 3, are on the fault trace. Fault-parallel motion is zero on the fault trace beyond the rupture.

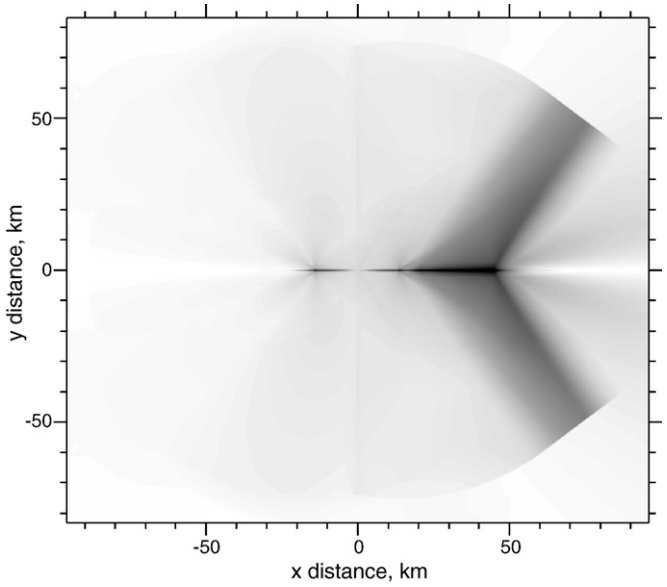

Fig. 7. Map of peak absolute value of the fault-parallel component of velocity in the 'supershear, soft stop' case, at times up to 30 s. Darkest shading is velocity of 5 m/s or greater.

beams propagating obliquely away from the fault. The beams are not diverging, so they are not attenuating. The terminations of the beams clearly show the planar Mach fronts at 30 s, the end of the calculation.

Time histories of velocity in the 'supershear, soft stop' case at three points in the Mach beam are shown in Fig. 9. Point M1 is at 48.25 km along strike and 12 km off fault, point M2 is 57 km along strike and 24 km off fault, and point M3 is at 65.75 km along strike and 36 km off fault. The Mach S wave is evident as large sharp spikes in both components of velocity. The Mach wave is superimposed on a P-wave that arrives earlier. The P-wave is different at the different points, but the change of velocity in the Mach wave is nearly the same.

Fig. 10 shows velocity time histories in the 'supershear, hard stop' case at the same three points in the Mach beam. The P-wave on which the Mach wave is superimposed differs subtly between the 'soft stop' and 'hard stop' cases, but the increments of velocity in the Mach wave are remarkably the same. The fault-parallel component of velocity increases by 2.125 ± 0.015 m/s, and the fault-normal component decreases by 1.55 ± 0.03 m/s in the abrupt step at the onset of the Mach wave in all six time histories. The direction of motion is transverse to the beam direction. The ratio of the components, $1.55/2.125 = 0.73$, agrees with the ratio expected from the rupture velocity, $\tan\phi = \tan(\sin^{-1}(1/1.677)) = 0.74$. The magnitude of the velocity change in the Mach wave is 2.63 m/s. Peak velocity in the directivity wave in the sub-Rayleigh case is larger than this out to distances greater than reached in these calculations.

The Mach wave depends only on the supershear propagation. It is independent of the stopping process, which affects the energy of other radiated waves.

These supershear calculations were repeated with smaller critical slip, $D_c = 0.346$ m. The amplitude of velocity in the Mach wave changed only slightly.

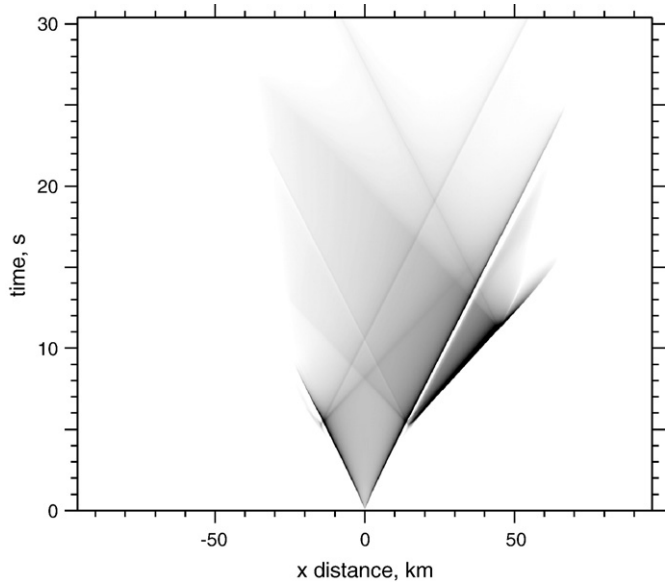

Fig. 6. Evolution of slip rate on the fault as a function of time in the 'supershear, soft stop' case. Darkest shading is slip rate of 5 m/s or greater.

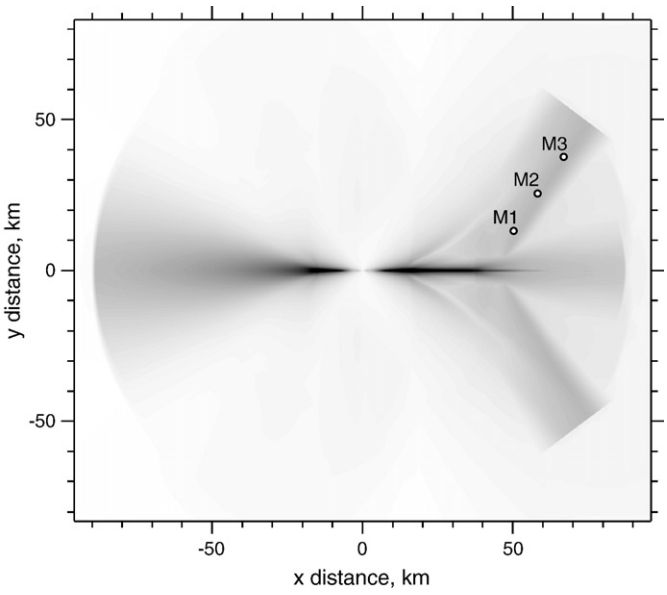

Fig. 8. Map of peak absolute value of the fault-normal component of velocity in the 'supershear, soft stop' case, at times up to 30 s. Darkest shading is velocity of 5 m/s or greater. Points labeled M1, M2, and M3 are locations of time histories shown in Figs. 9 and 10.

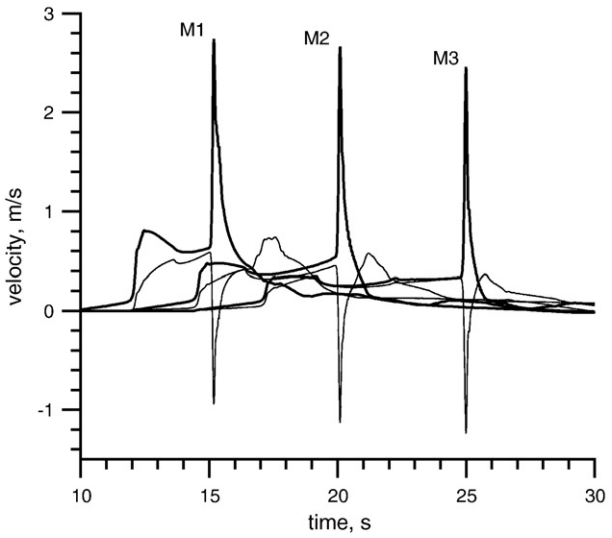

Fig. 9. Time histories of both components of velocity in the 'supershear, soft stop' case at points M1, M2, and M3. Locations are shown in Fig. 8. Heavy curves with positive spikes: fault-parallel component; light curves with negative spikes: fault-normal component. The direction of motion in the Mach S wave is transverse to the beam direction.

5. Discussion

These elastic 2D calculations could have been done with non-dimensional units. Choices made here of dimensional units are arbitrary, and the solutions may be scaled in two different ways. First is amplitude scaling, in which stress drop is multiplied by a scale factor. Material velocity and slip rate are multiplied by the same factor, while propagation velocity remains the same. The second is length scaling. If all lengths, including input such as D_c and the grid interval, are multiplied by a scale factor, and time is multiplied by the same factor, then stress and velocity remain unchanged at scaled space-time points. The resulting slip and supershear transition length will be multiplied by the scale factor. In a 3D problem, the variation of properties with depth would fix a length scale, and the termination of slip with depth would limit slip values in long ruptures. The ridiculously large slip values found here could be reduced by reducing the length scale, but there is no pretense that these 2D results could represent a 3D solution.

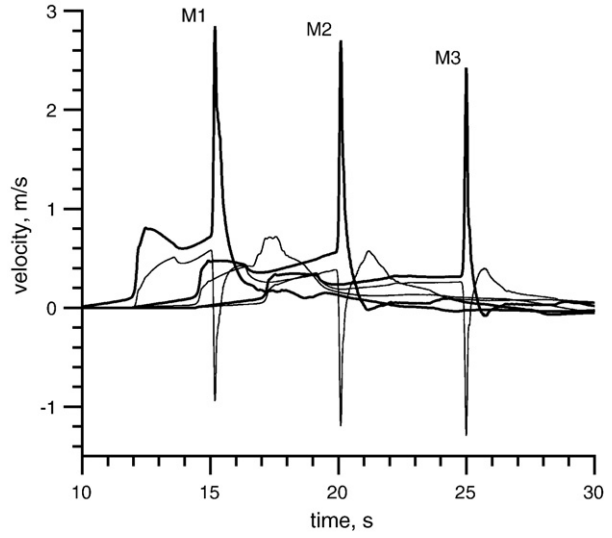

Fig. 10. Time histories of both components of velocity in the 'supershear, hard stop' case at points M1, M2, and M3. Locations are shown in Fig. 8. Heavy curves with positive spikes: fault-parallel component; light curves with negative spikes: fault-normal component.

The dynamic stress drop chosen here, 10 MPa, is within the range of observed values, although on the high side. Therefore, the amplitude scaling is appropriate. The resulting peak velocities, however, are far larger than observed in actual earthquakes. The reason is that these sources are coherent, with smooth propagation near the terminal rupture velocities. Signals from different points on the fault surface add coherently at the wave fronts, in both the directivity pulse in the sub-Rayleigh case and the Mach wave in the supershear case. These results exhibit the maximum directivity effect.

For smaller sub-Rayleigh rupture velocity, the amplitude of the directivity pulse will be smaller. Similarly, for smaller supershear rupture velocity with the same stress drop, the amplitude of the Mach wave will be smaller (Dunham and Bhat, 2008). The comparison made here is for idealized cases in which the rupture velocity is very near the terminal velocity. A comparison could be made with larger fracture energy, so that rupture velocities would be more realistic, but that comparison has not been made in this work.

Existence of supershear rupture does not guarantee a strong Mach wave. That depends on the coherence of the rupture. Evidence from actual earthquakes indicates that stress drop is heterogeneous and propagation is irregular at all length scales. With irregular propagation, radiation from different elements of the fault will be incoherent, and the large peak values of velocity will be reduced in both the directivity pulse and the Mach wave. In order to make these idealized problems more realistic, it is necessary, not only to change from 2D to 3D, but also to use heterogeneous stress drop and propagation, as is being done by Schmedes et al. (2009) and Bizzarri et al. (2010).

In empirical studies, the directivity effect is observed to decrease with decreasing period, and is absent at periods shorter than 1 s (Somerville et al., 1997). Therefore, real sources are incoherent at short period. The Mach wave calculated here consists of periods shorter than 1 s. In empirical fits to ground motion attenuation, stations within expected Mach beams do not have enhanced amplitude (Bizzarri et al., 2010), which may mean that earthquake sources are too heterogeneous for strong Mach waves to exist.

The directivity pulse in the sub-Rayleigh case attenuates due to geometric spreading, even though it is confined to a small range of azimuths. The Mach wave, on the other hand, is a beam of parallel rays. Such a beam is eventually subject to geometrical spreading due to diffraction. Intensity is not constant across the Mach beam, because its source, slip rate, is growing as the rupture propagates. (Note that locations of the time histories in the Mach wave were chosen to be near a single ray in the beam.) For the sake of a simple analysis, however, suppose that intensity is constant across a beam with initial width D_0. Due to diffraction, a component with wavelength λ will have an angular spread of propagation directions of $\alpha = \lambda/D_0$. The beam width of that component at distance R is $D = D_0 + (\lambda/D_0)R = D_0(1 + \lambda R/D_0^2)$. Therefore, geometrical spreading becomes important for the component with wavelength λ at distance $R = D_0^2/\lambda$. Longer wavelength components will diffract and spread sooner than shorter wavelength components. The beam width is about 20 km, and wavelengths in the Mach pulse are less than 3 km, so no attenuation is seen in these calculations. The beam will eventually attenuate, with the shortest wavelengths persisting longest. The shorter wavelengths, however, will be depleted in an irregular source and are more subject to scattering. Therefore, attenuation of a Mach wave is determined by heterogeneity in both the source and the medium.

An estimate of the importance of diffraction may be made for a coherent source and a regional attenuation model in which amplitudes are multiplied by $\exp(-\pi Q_S^{-1} R/\lambda)$. This attenuation factor becomes important at $\pi R/Q_S\lambda = 1$. Geometric spreading due to diffraction becomes important at $R\lambda/D_0^2 = 1$. Solving this pair of equations simultaneously yields the λ, R pair of the longest persisting component

in the Mach wave. For $Q_S = 200$, $D_0 = 20$ km, and $v_S = 3$ km/s, the distance reached by this longest persisting component is $R = 160$ km, and the wavelength is 2.5 km, or frequency is 1.2 Hz. Shorter wavelengths are absorbed or scattered, and longer wavelengths diffract. The Mach waves in these calculations consist primarily of frequencies higher than 1 Hz. Therefore the Mach wave will be attenuated by scattering and absorption before diffraction is effective. This estimate assumes a perfectly coherent beam.

Sources with equal radiated energy will have the same average ground motion hazard (neglecting different spectral shape) as a function of distance from the source. In empirical attenuation relations that depend on distance alone, the existence of the directivity beam or the Mach beam will increase the variance. The directivity beam increases variance in sub-Rayleigh events near the fault. The Mach beam increases variance in supershear events at greater distance. The idealized results found here are only limiting cases. Coherence expected in actual events can only be found from observations.

6. Conclusion

Maps of peak ground velocity are compared for events with sub-Rayleigh and supershear rupture velocity for idealized 2D models with the same stress drop, fracture energy, and rupture length. Ruptures are coherent, smooth, and approach the limiting velocities, so that directivity effects are maximized. These are not realistic sources, because there is no heterogeneity of stress drop and rupture propagation. In each case, the radiated energy is focused into a beam. In the sub-Rayleigh case, the directivity beam is concentrated in a narrow range of azimuths around the fault projection. Peak velocity, originally very intense, attenuates in this beam, because the beam is diverging. In the supershear case, the Mach wave forms a beam of parallel rays. The Mach beam may also be considered a directivity effect, because it depends on the coherence of the source. The Mach wave has constant amplitude until, at greater distance, it attenuates due to diffraction and scattering. The Mach wave has smaller amplitude than the directivity pulse near the fault.

Mach waves have not been observed. Real earthquake sources may be too heterogeneous to generate strong Mach waves.

Acknowledgement

I am grateful for constructive reviews by Paul Spudich and Jack Boatwright.

References

Andrews, D.J., 1976. Rupture velocity of plane strain shear cracks. J. Geophys. Res. 81, 5679–5687.
Archuleta, R.J., 1984. A faulting model for the 1979 Imperial Valley earthquake. J. Geophys. Res. 89, 4559–4586.
Bernard, P., Baumont, D., 2005. Shear Mach wave characterization for kinematic fault rupture models with constant supershear rupture velocity. Geophys. J. Int. 162, 431–447.
Bizzarri, A., Spudich, P., 2008. Effects of super-shear rupture speed on the high frequency content of S-waves investigated using spontaneous dynamic rupture models and isochrone theory. J. Geophys. Res. 113. doi:10.1029/2007JB005146.
Bizzarri, A., E. M. Dunham, and P. Spudich, 2010. Coherence of Mach fronts during heterogeneous supershear earthquake rupture propagation. J. Gephys. Res. doi:10.1029/2009JB006819.
Burridge, R., 1973. Admissible speeds for plane-strain self-similar shear cracks with friction but lacking cohesion. Geophys. J. Roy. Astron. Soc. 35, 439–455.
Dunham, E.M., Archuleta, R.J., 2005. Near-source ground motion from steady state dynamic rupture pulses. Geophys. Res. Lett. 32, L03302.
Dunham, E.M., Bhat, H.S., 2008. Attenuation of radiated ground motion and stresses from three-dimensional supershear ruptures. J. Geophys. Res. 113, B08319. doi:10.1029/2007JB005182.
Kostrov, B.V., 1970. The theory of the focus for tectonic earthquakes, Izv. Acad. Sci. USSR Phys. Solid Earth. Engl. Transl. No. 4, 258–267.
Liu, Y., Lapusta, N., 2008. Transition of mode II cracks from sub-Rayleigh to intersonic speeds in the presence of favorable heterogeneity. J. Mech. Phys. Solids 56, 25–50.
Schmedes, J., Archuleta, R.J., Lavallee, D., 2009. Dependency of supershear transition in dynamic rupture simulations on the autocorrelation of initial stress (abstract). Seismol. Res. Lett. 80 (2), 301.
Somerville, P.G., Smith, N.F., Graves, R.W., Abrahamson, N.A., 1997. Modification of empirical strong ground motion attenuation relations to include the amplitude and duration effects of rupture directivity. Seismolog. Res. Lett. 68, 199–222.
Spudich, P., Cranswick, E., 1984. Direct observation of rupture propagation during the 1979 Imperial Valley earthquake using a short baseline accelerometer array. Bull. Seismol. Soc. Am. 74, 2083–2114.